We are IntechOpen, the world's leading publisher of Open Access books Built by scientists, for scientists

6,900
Open access books available

186,000
International authors and editors

200M
Downloads

Our authors are among the

154
Countries delivered to

TOP 1%
most cited scientists

12.2%
Contributors from top 500 universities

CLARIVATE ANALYTICS
BOOK CITATION INDEX
INDEXED

WEB OF SCIENCE™

Selection of our books indexed in the Book Citation Index
in Web of Science™ Core Collection (BKCI)

Interested in publishing with us?
Contact book.department@intechopen.com

Chapter

Monitoring of Tsunami/ Earthquake Damages by Polarimetric Microwave Remote Sensing Technique

Dong Li, Yunhua Zhang, Liting Liang, Jiefang Yang and Xun Wang

Abstract

Polarization characterizes the vector state of EM wave. When interacting with polarized wave, rough natural surface often induces dominant surface scattering; building also presents dominant double-bounce scattering. Tsunami/earthquake causes serious destruction just by inundating the land surface and destroying the building. By analyzing the change of surface and double-bounce scattering before and after disaster, we can achieve a monitoring of damages. This constitutes one basic principle of polarimetric microwave remote sensing of tsunami/earthquake. The extraction of surface and double-bounce scattering from coherency matrix is achieved by model-based decomposition. The general four-component scattering power decomposition with unitary transformation (G4U) has been widely used in the remote sensing of tsunami/earthquake to identify surface and double-bounce scattering because it can adaptively enhance surface or double-bounce scattering. Nonetheless, the strict derivation in this chapter conveys that G4U cannot always strengthen the double-bounce scattering in urban area nor strengthen the surface scattering in water or land area unless we adaptively combine G4U and its duality for an extended G4U (EG4U). Experiment on the ALOS-PALSAR datasets of 2011 great Tohoku tsunami/earthquake demonstrates not only the outperformance of EG4U but also the effectiveness of polarimetric remote sensing in the qualitative monitoring and quantitative evaluation of tsunami/earthquake damages.

Keywords: disaster monitoring, damage evaluation, tsunami, earthquake, microwave remote sensing, synthetic aperture radar (SAR), polarimetric SAR (PolSAR), polarimetric decomposition, scattering model, unitary transformation

1. Introduction

Tsunami and earthquake seriously endanger people's lives and properties. Efficient and accurate monitoring and assessment are of crucial importance for the fast response, management, and mitigation of the disasters [1–3]. Compared with the optical remote sensing, microwave remote sensing technology such as synthetic aperture radar (SAR) has been widely applied to monitoring natural and human-induced disasters for its all-day and all-weather working capacity [4].

Polarization is an essential property of the electromagnetic wave [5–8]. The polarization state of wave will change when interacting with ground object. For example, rough natural surface such as land and water often induces the strong Bragg surface scattering, while building often presents the dominant double-bounce scattering because of the dihedral corner reflectors formed by ground and the vertical wall of building. Therefore, by analyzing the polarization of the scattering wave, we can acquire the physical and geometrical information regarding the object. This is the main task of SAR polarimetry (PolSAR) [9–11].

Tsunami is often accompanied by earthquake and flooding [1–3]. It damages and inundates the buildings and causes the collapse of the ground-wall dihedral structures as well as the enhancement of the direct surface scatterers. Therefore, by analyzing the power of double-bounce scattering and surface scattering before and after the event, we can achieve an efficient monitoring of the disasters. This simple strategy has been successfully adopted in the polarimetric microwave remote sensing of tsunami/earthquake [12–21].

Nonetheless, the extraction of double-bounce scattering and surface scattering from PolSAR image is not so straightforward because each pixel in PolSAR is a 3×3 complex coherency matrix $\langle[T]\rangle$ with nine degrees of freedom (DoF). A widely used approach to achieve this is to decompose $\langle[T]\rangle$ on the canonical scattering models [22]. The first such decomposition was devised by Freeman and Durden [23] which expands $\langle[T]\rangle$ on the surface scattering, double-bounce scattering, and volume scattering (describes the complex scattering in vegetation area). This three-component decomposition, however, is responsible for only five DoF of $\langle[T]\rangle$ because of the symmetric reflection assumption. This assumption was tackled by Yamaguchi et al. [24] by introducing a fourth helix component and two additional models of volume scattering. The resulted four-component decomposition (Y4O) then only leaves three DoF unaccounted: the $(1, 3)$ element of $\langle[T]\rangle$, i.e., T_{13}, and the real part of the $(2, 3)$ element of $\langle[T]\rangle$, i.e., $\mathrm{Re}\{T_{23}\}$. A same target will present differently by a simple rotation about the line of sight of radar. Deorientation should be first conducted on $\langle[T]\rangle$ to eliminate the influence [25]. As a result, $\mathrm{Re}\{T_{23}\}$ changes to zero and Y4O with rotation (Y4R) accounts for seven DoF [26]. Based on Y4R, Sato et al. [27] further proposed to add a new model to characterize volume scattering generated by even-bounce structure. However, Sato's extended Y4R (S4R) still leaves T_{13} unaccounted. To solve this, Singh et al. [28] in 2013 proposed a general four-component decomposition (G4U) based on a special unitary matrix. G4U enables T_{13} included in the accounted models by conducting unitary transformation to the rotated version of $\langle[T]\rangle$. Singh et al. [28] claimed that G4U could make full use of polarimetric parameters. As a result, in comparison with the four-component decompositions such as S4R and Y4R, G4U could enhance double-bounce scattering power over urban area while enhancing surface scattering contribution over an area where surface scattering is preferable [28]. This makes G4U very suitable to the remote sensing of tsunami/earthquake [16, 20] and establishes G4U the state-of-the-art four-component scattering power decomposition [29, 30].

This chapter is dedicated to enable an extension to G4U for better monitoring of tsunami/earthquake disaster. It is indicated that the unitary transformation in G4U adds a T_{13}-related but redundant balance equation to the original self-contained equation system in Y4R and S4R. Then T_{13} is accounted for by G4U, but we obtain no exact solution to the system but the approximate ones. The general expression of the approximate solutions enables a generalized G4U (GG4U), while G4U and S4R represent two special forms. A dual G4U (DG4U) is also obtained. The general solution indicates that G4U cannot always enhance the double-bounce scattering power over urban area nor strengthen the surface scattering power over the area where surface scattering is dominant unless we adaptively integrate G4U

and DG4U for an extended G4U (EG4U). Experiments on the PolSAR images of Miyagi Prefecture, Japan, acquired by the L-band spaceborne ALOS-PALSAR system before and after the March 11, 2011, Off-Tohoku 9.0 tsunami/earthquake demonstrate not only the outperformance of EG4U but also the effectiveness of polarimetric remote sensing in the monitoring of tsunami/earthquake disaster.

The remainder of this chapter is arranged as follows. Section 2 presents the basic principle of PolSAR and the polarization descriptors first. The advanced four-component scattering power decompositions are then described in Section 3 to develop the EG4U. By decomposing the ALOS-PALSAR datasets of the 2011 great Tohoku tsunami/earthquake using EG4U, Section 4 evaluates and analyzes the polarimetric monitoring of disaster damages further. The chapter is eventually concluded in Section 5.

2. SAR polarimetry and polarization descriptors

SAR is an active microwave remote sensing technique dedicated to acquire the large-scaled 2D coherent image of the earth's surface reflectivity [9]. It transmits microwave pulses and receives the backscattering from the illuminated terrain to synthesize a high spatial resolution image. Such an active operation enables SAR an all-day working capacity independent of solar illumination. In addition, operating in the microwave region of electromagnetic spectrum avoids the effects of rain and clouds, which allows SAR an almost all-weather continuous monitoring of the earth surface [9].

Polarization characterizes the vector state of the electromagnetic wave. The polarization state of wave will change when interacting with a ground object. By processing and analyzing such change of polarization, we can obtain the material, roughness, shape, and orientation information regarding the object. The core of this change is the (Sinclair) scattering matrix $[S]$ of the object, which transforms the incident electric filed E^I into the scattered electric filed E^S [31]:

$$E^S = \frac{e^{-jkr}}{r}[S]E^I \rightarrow \begin{bmatrix} E_H^S \\ E_V^S \end{bmatrix} = \frac{e^{-jkr}}{r} \begin{bmatrix} S_{HH} & S_{HV} \\ S_{VH} & S_{VV} \end{bmatrix} \begin{bmatrix} E_H^I \\ E_V^I \end{bmatrix} \tag{1}$$

where r denotes the distance from radar to ground object, k is the wave number, and subscript H or V represents the horizontal or vertical polarization. Matrix $[S]$ is obtained by first transmitting H-polarized wave (E_H^I) and receiving scatterings in H - and V-polarization simultaneously to measure the first column S_{HH} and S_{VH} and then transmitting V-polarized wave (E_V^I) and also receiving in H- and V-polarization simultaneously for the second column S_{HV} and S_{VV}. In reciprocal backscattering, we have $S_{HV} = S_{VH}$ and matrix $[S]$ covers five DoF then.

Generally, almost all the ground scatterers are situated in the dynamically changing environment and subjected to spatial and/or temporal variations [32]. Such scatterer is called the distributed target, and we can no longer model its scattering with a determined scattering matrix $[S]$. The 3×3 coherency matrix $\langle [T] \rangle$ is then constructed as the statistical average of the acquired scatterings to describe the second-order moment of the fluctuations [9]:

$$\langle [T] \rangle = \langle \boldsymbol{kk}^\dagger \rangle = \begin{bmatrix} T_{11} & T_{12} & T_{13} \\ T_{21} & T_{22} & T_{23} \\ T_{31} & T_{32} & T_{33} \end{bmatrix}, \boldsymbol{k} = \frac{1}{\sqrt{2}} \begin{bmatrix} S_{HH} + S_{VV} \\ S_{HH} - S_{VV} \\ 2S_{HV} \end{bmatrix} \tag{2}$$

where $\langle \cdot \rangle$ and superscript $\dagger$ represent the operations of ensemble average and conjugate transpose and $\boldsymbol{k}$ denotes the Pauli vector. The spatial/temporal depolarization pushes the DoF of $\langle [T] \rangle$ to nine. Therefore, different from the conventional SAR image, each pixel in PolSAR image is not a complex number but a 3×3 coherency matrix $\langle [T] \rangle$.

The coherency matrix $\langle [T] \rangle$ in Eq. (2) is expressed in the H-V polarization basis; we can also formulate it in some other orthonormal basis by simply taking the unitary transformation of $\langle [T] \rangle$:

$$\text{Unitary}(\langle [T] \rangle) \stackrel{\text{def}}{=} [U_3]\langle [T] \rangle [U_3]^{\dagger} \tag{3}$$

where $[U_3]$ is the special unitary matrix that describes the relationship between H-V and the new orthonormal basis. Target deorientation is just based on the real rotation matrix [25]:

$$[U_3(\theta)] = \begin{bmatrix} 1 & 0 & 0 \\ 0 & \cos 2\theta & \sin 2\theta \\ 0 & -\sin 2\theta & \cos 2\theta \end{bmatrix}, 2\theta = \frac{1}{2}\tan^{-1}\left(\frac{2\,\text{Re}\,\{T_{23}\}}{T_{22} - T_{33}}\right) \tag{4}$$

Combining Eq. (4) into Eq. (3), the deoriented coherency matrix $\langle [T'] \rangle$ is

$$\langle [T'] \rangle = [U_3(\theta)]\langle [T] \rangle [U_3(\theta)]^{\dagger} = \begin{bmatrix} T'_{11} & T'_{12} & T'_{13} \\ T'_{21} & T'_{22} & j\text{Im}\{T'_{23}\} \\ T'_{31} & j\text{Im}\{T'_{32}\} & T'_{33} \end{bmatrix}. \tag{5}$$

Deorientation makes T'_{23} become purely imaginary and reduces DoF from nine to eight. In order to eliminate the imaginary part further, Singh et al. developed an imaginary rotation matrix [28]:

$$[U_3(\varphi)] = \begin{bmatrix} 1 & 0 & 0 \\ 0 & \cos 2\varphi & j\sin 2\varphi \\ 0 & j\sin 2\varphi & \cos 2\varphi \end{bmatrix}, 2\varphi = \frac{1}{2}\tan^{-1}\left(\frac{2\text{Im}\{T'_{23}\}}{T'_{22} - T'_{33}}\right). \tag{6}$$

A coherency matrix $\langle [T''] \rangle$ with zero T''_{23} is then achieved:

$$\langle [T''] \rangle = [U_3(\varphi)]\langle [T'] \rangle [U_3(\varphi)]^{\dagger} = \begin{bmatrix} T''_{11} & T''_{12} & T''_{13} \\ T''_{21} & T''_{22} & 0 \\ T''_{31} & 0 & T''_{33} \end{bmatrix}. \tag{7}$$

3. Advanced four-component scattering power decompositions

Polarimetric incoherent decomposition plays an important role in the discrimination and recognition of the distributed target [22]. It pursues the scattering mechanism of the unknown target by extracting the dominant or average target (such as the Huynen-type phenomenological dichotomies [7, 32] and the eigenvalue/eigenvector-based target decompositions [9, 33]) from $\langle [T] \rangle$ or expanding $\langle [T] \rangle$ on the canonical models (such as the model-based target decompositions [23–28]). Among these decompositions, the four-component scattering power decompositions such as Y4R, S4R, and G4U have been a hot topic recently [29].

3.1 Y4R and S4R

Y4R and S4R decompose the target by linearly expanding matrix $\langle [T'] \rangle$ on the four canonical scattering models, as illustrated in **Figure 1**:

$$\langle [T'] \rangle = f_S \langle [T'_S] \rangle + f_D \langle [T'_D] \rangle + f_V \langle [T'_V] \rangle + f_C \langle [T'_C] \rangle \tag{8}$$

where $\langle [T'_S] \rangle$, $\langle [T'_D] \rangle$, $\langle [T'_V] \rangle$, and $\langle [T'_C] \rangle$ denote the surface scattering model, the double-bounce scattering model, the volume scattering model, and the helix scattering model, respectively:

$$\langle [T'_S] \rangle = \begin{bmatrix} 1 & \beta & 0 \\ \beta^* & |\beta|^2 & 0 \\ 0 & 0 & 0 \end{bmatrix}, \langle [T'_D] \rangle = \begin{bmatrix} |\alpha|^2 & \alpha & 0 \\ \alpha^* & 1 & 0 \\ 0 & 0 & 0 \end{bmatrix},$$

$$\langle [T'_V] \rangle = \begin{bmatrix} a & d & 0 \\ d & b & 0 \\ 0 & 0 & c \end{bmatrix}, \langle [T'_C] \rangle = \frac{1}{2} \begin{bmatrix} 0 & 0 & 0 \\ 0 & 1 & \pm j \\ 0 & \mp j & 1 \end{bmatrix}. \tag{9}$$
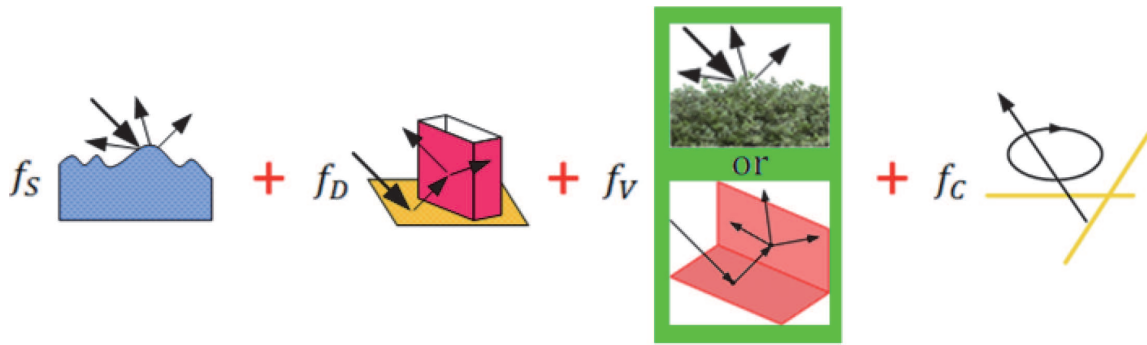

Figure 1.
The canonical models involved in the four-component model-based scattering power decompositions.

Parameters f_S, f_D, f_V, and f_C in Eq. (8) represent the contributions of the four components; β and α in $\langle [T'_S] \rangle$ and $\langle [T'_D] \rangle$ are complex parameters; a, b, c, and d in $\langle [T'_V] \rangle$ are real constants satisfying $a + b + c = 1$, which involve in four volume scattering models and are adaptively selected according to the branch conditions [27, 28]. Combining Eqs. (8) and (9), the S4R/Y4R scattering balance equation system on unknowns f_S, f_D, f_V, f_C, α, and β is formulated [26, 27]:

$$\begin{cases} f_S + f_D |\alpha|^2 + f_V a = T'_{11} & - 1) \\ f_S \beta + f_D \alpha + f_V d = T'_{12} & - 2) \\ f_S |\beta|^2 + f_D + f_V b + \dfrac{f_C}{2} = T'_{22} & - 3) \\ \pm j \dfrac{f_C}{2} = j\,\mathrm{Im}\{T'_{23}\} & - 4) \\ f_V c + \dfrac{f_C}{2} = T'_{33} & - 5) \end{cases} \tag{10}$$

Nevertheless, we obtain no scattering balance equation on T'_{13} in Eq. (10). Hence, there always exists a T'_{13}-related unaccounted residue in Y4R and S4R.

3.2 G4U

To model T'_{13}, G4U uses $[U_3(\varphi)]$ to conduct unitary transformation to both sides of Eq. (10) first and then eliminates the influence of φ [28]. As a result, an additional balance equation is brought into G4U, and we obtain the following scattering balance equation system [30]:

$$\begin{cases} f_S + f_D|\alpha|^2 + f_V a = T'_{11} & -1) \\ \left.\begin{array}{l} f_S\beta + f_D\alpha + f_V d = T'_{12} + T'_{13} \\ f_S\beta + f_D\alpha + f_V d = T'_{12} - T'_{13} \end{array}\right\} & -2) \\ f_S|\beta|^2 + f_D + f_V b + \dfrac{f_C}{2} = T'_{22} & -3) \\ \pm j\dfrac{f_C}{2} = j\mathrm{Im}\{T'_{23}\} & -4) \\ f_V c + \dfrac{f_C}{2} = T'_{33} & -5) \end{cases} \tag{11}$$

Comparing Eq. (11) with Eq. (10), we can find that Eq. (11–2) gives a dichotomy to Eq. (10–2). The redundancy makes Eq. (11) have no such exact solution like Eq. (10) but some approximate ones. In G4U, Singh et al. preferred the first equation of (11–2) only.

3.3 GG4U: generalization of G4U

Obviously, Eq. (11) provides us a generalized G4U (GG4U). Here we focus on the general solution to (11) for the unknowns f_S, f_D, f_V, f_C, α, and β. Let

$$\begin{cases} S = T'_{11} - f_V a \\ C_1 = T'_{12} + T'_{13} - f_V d \\ C_2 = T'_{12} - T'_{13} - f_V d \\ D = T'_{22} - f_V b - \dfrac{f_C}{2} \\ C = \dfrac{1+\mu}{2}C_1 + \dfrac{1-\mu}{2}C_2 \end{cases} \tag{12}$$

where μ is a real constant. Then Eq. (11) can be rearranged as

$$\begin{cases} f_S + f_D|\alpha|^2 = S & -1) \\ f_S\beta + f_D\alpha = C & -2) \\ f_S|\beta|^2 + f_D = D & -3) \\ f_C = 2|\mathrm{Im}\{T'_{23}\}| & -4) \\ f_V = \dfrac{1}{2c}(2T'_{33} - f_C) & -5) \end{cases} \tag{13}$$

Eq. (13) comprises of five equations and six unknowns. Following Freeman-Durden [23] and Yamaguchi et al. [24], we can fix α or β in terms of the sign of $S - D$ for the superior between surface scattering and double-bounce scattering:

$$\begin{cases} \quad BC > 0 \Rightarrow \text{dominant surface scattering} \Rightarrow \alpha = 0 \\ BC \le 0 \Rightarrow \text{dominant double} - \text{bounce scattering} \Rightarrow \beta = 0 \end{cases} \tag{14}$$

where $BC = S - D$. Combining Eqs. (13) and (14), we can then simply obtain the scattering power of each of the four components, i.e., the surface scattering power P_S, the double-bounce scattering power P_D, the volume scattering power P_V, and the helix scattering power P_C:

$$\begin{cases} P_S = f_S\left(1 + |\beta|^2\right) = \begin{cases} S + \dfrac{|C|^2}{S}, BC > 0 \\ S - \dfrac{|C|^2}{D}, BC \le 0 \end{cases} \\ P_D = f_D\left(1 + |\alpha|^2\right) = \begin{cases} D - \dfrac{|C|^2}{S}, BC > 0 \\ D + \dfrac{|C|^2}{D}, BC \le 0 \end{cases} \\ P_C = f_C H\left(T'_{33} - |\text{Im}\{T'_{23}\}|\right) \\ P_V = \dfrac{1}{2c}\left(2T'_{33} - P_C\right) \end{cases} \tag{15}$$

where $H(\cdot)$ denotes the Heaviside step function, which is used here to adjust the value of P_C for nonnegative P_V ruling [27]. It can be easily validated that $P_S + P_D + P_V + P_C = T'_{11} + T'_{22} + T'_{33}$. Thus GG4U gives a decomposition of scattering power.

3.4 Special decompositions

By taking appropriate value to μ, we can have some different decompositions, which are denoted as $\mathcal{G}(\mu)$. Here we are particularly interested to the following special cases of $\mathcal{G}(\mu)$.

Case (1): $\mathcal{G}(+1) := \text{G4U}$

$$C = C_1 = T'_{12} + T'_{13} - f_V d = C_{\text{G4U}}. \tag{16}$$

This is just the parameter C used in G4U. GG4U changes to G4U in this case.

Case (2): $\mathcal{G}(-1) := \text{DG4U}$

$$C = C_2 = T'_{12} - T'_{13} - f_V d. \tag{17}$$

This acts as the complement of case (1); thus we name it the dual G4U (DG4U).

Case (3): $\mathcal{G}(0) := \text{S4R}$

$$C = \frac{C_1 + C_2}{2} = T'_{12} - f_V d = C_{\text{S4R}}. \tag{18}$$

This is the parameter C used in S4R, i.e., S4R also shows a special form of GG4U. Hence, the essential difference between S4R and G4U just lies in the different definition of parameter C in Eqs. (16) and (18). The unitary transformation is just

to enable the T'_{13} entry contained in C_{G4U} and finally in P_S and P_D. Parameter C defined in Eq. (12) is a generalization of C_{G4U} and C_{S4R}.

3.5 Theoretical evaluation of S4R and G4U

S4R can improve Y4R by strengthening the double-bounce scattering in urban area [27]. Singh et al. [28] indicated that G4U could further improve S4R in this aspect by strengthening surface scattering in the area where surface scattering is preferable to double-bounce scattering, while increasing the double-bounce scattering in the urban area where the double-bounce scattering is preferable to surface scattering. By combining the ruling in Eq. (14), we can formulate these observations as

$$\begin{cases} P_S^{\text{G4U}} \geq P_S^{\text{S4R}}, BC > 0 \\ P_D^{\text{G4U}} \geq P_D^{\text{S4R}}, BC \leq 0 \end{cases}. \tag{19}$$

In terms of the general expression of P_S and P_D in (15), here we give a simple validation to Eq. (19) by combining $\mu = 0$ and $\mu = 1$ into Eqs. (12) and (15):

$$\begin{cases} P_S^{\text{G4U}} = S + \dfrac{|C_1|^2}{S} \\ P_S^{\text{S4R}} = S + \dfrac{|C_1 + C_2|^2}{4S} \end{cases}, BC > 0; \quad \begin{cases} P_D^{\text{G4U}} = D + \dfrac{|C_1|^2}{D} \\ P_D^{\text{S4R}} = D + \dfrac{|C_1 + C_2|^2}{4D} \end{cases}, BC \leq 0. \tag{20}$$

From Eq. (20) we have

$$\begin{cases} P_S^{\text{G4U}} - P_S^{\text{S4R}} = \dfrac{|2C_1|^2 - |C_1 + C_2|^2}{4S}, BC > 0 \\ P_D^{\text{G4U}} - P_D^{\text{S4R}} = \dfrac{|2C_1|^2 - |C_1 + C_2|^2}{4D}, BC \leq 0 \end{cases}. \tag{21}$$

Then Eq. (19) will hold if $|2C_1|^2 - |C_1 + C_2|^2 \geq 0$. Obviously, this condition is not always tenable. Hence, despite better performance in some areas, G4U cannot improve S4R for every target area. To tackle this, the extended G4U (EG4U) will be developed in the following as an adaptive combination of G4U and DG4U.

3.6 EG4U: adaptive combination of G4U and DG4U

Combining $\mu = -1$ into Eqs. (12) and (15), DG4U surface and double-bounce scattering powers can be formulated as

$$\begin{cases} P_S^{\text{DG4U}} = S + \dfrac{|C_2|^2}{S}, BC > 0 \\ P_D^{\text{DG4U}} = D + \dfrac{|C_2|^2}{D}, BC \leq 0 \end{cases}. \tag{22}$$

Combining Eqs. (20) and (22), after some simple deduction, we obtain

$$\begin{cases} \dfrac{P_S^{\text{G4U}} + P_S^{\text{DG4U}}}{2} - P_S^{\text{S4R}} = \dfrac{|C_1 - C_2|^2}{4S} \geq 0, BC > 0 \\ \dfrac{P_D^{\text{G4U}} + P_D^{\text{DG4U}}}{2} - P_D^{\text{S4R}} = \dfrac{|C_1 - C_2|^2}{4D} \geq 0, BC \leq 0 \end{cases} \tag{23}$$

$$\begin{cases} P_S^{\text{G4U}} - P_S^{\text{DG4U}} = \dfrac{|C_1|^2 - |C_2|^2}{S}, BC > 0 \\[3mm] P_D^{\text{G4U}} - P_D^{\text{DG4U}} = \dfrac{|C_1|^2 - |C_2|^2}{D}, BC \leq 0 \end{cases}. \tag{24}$$

We can immediately obtain from Eq. (23) that

$$\begin{cases} \max\left\{P_S^{\text{G4U}}, P_S^{\text{DG4U}}\right\} \geq P_S^{\text{S4R}}, BC > 0 \\[2mm] \max\left\{P_D^{\text{G4U}}, P_D^{\text{DG4U}}\right\} \geq P_D^{\text{S4R}}, BC \leq 0 \end{cases}. \tag{25}$$

From Eq. (24) we obtain

$$\begin{cases} \begin{cases} \max\left\{P_S^{\text{G4U}}, P_S^{\text{DG4U}}\right\} = P_S^{\text{G4U}}, BC > 0 \\[2mm] \max\left\{P_D^{\text{G4U}}, P_D^{\text{DG4U}}\right\} = P_D^{\text{G4U}}, BC \leq 0 \end{cases}, BC_1 > 0 \\[8mm] \begin{cases} \max\left\{P_S^{\text{G4U}}, P_S^{\text{DG4U}}\right\} = P_S^{\text{DG4U}}, BC > 0 \\[2mm] \max\left\{P_D^{\text{G4U}}, P_D^{\text{DG4U}}\right\} = P_D^{\text{DG4U}}, BC \leq 0 \end{cases}, BC_1 \leq 0 \end{cases} \tag{26}$$

where $BC_1 = |C_1| - |C_2|$. Eq. (26) just lays the foundation for EG4U:

$$\text{EG4U} := \mathcal{G}(\pm 1) = \begin{cases} \mathcal{G}(+1) = \text{G4U}, BC_1 > 0 \\[2mm] \mathcal{G}(-1) = \text{DG4U}, BC_1 \leq 0 \end{cases}. \tag{27}$$

As the adaptive combination of G4U and DG4U, EG4U is also a special case of GG4U. So we denote it as $\mathcal{G}(\pm 1)$. By bringing $\mu = +1$ or $\mu = -1$ into Eqs. (12) and (15) based on the branch condition BC_1, we can achieve the scattering powers of four components in EG4U. Furthermore, from Eqs. (25) to (27), we have

$$\begin{cases} P_S^{\text{EG4U}} = \max\left\{P_S^{\text{G4U}}, P_S^{\text{DG4U}}\right\} \geq \left\{P_S^{\text{S4R}}, P_S^{\text{G4U}}, P_S^{\text{DG4U}}\right\}, BC > 0 \\[2mm] P_D^{\text{EG4U}} = \max\left\{P_D^{\text{G4U}}, P_D^{\text{DG4U}}\right\} \geq \left\{P_D^{\text{S4R}}, P_D^{\text{G4U}}, P_D^{\text{DG4U}}\right\}, BC \leq 0 \end{cases}. \tag{28}$$

Compared with S4R and G4U, EG4U increases surface scattering in area where surface scattering is superior to double-bounce scattering and strengthens double-bounce scattering in area where double-bounce scattering is preferable to surface scattering. Therefore, EG4U achieves not only a nice improvement to S4R, but also an effective extension to G4U. This may make EG4U more suitable to the remote sensing of tsunami/earthquake. We will investigate this in Section 4. The procedure of EG4U is outlined in **Algorithm 1**.

Algorithm 1: EG4U

01: Input: $\langle[T]\rangle$
02: Conduct deorientation to $\langle[T]\rangle$ for $\langle[T']\rangle$
03: Compute helix power $P_C = 2\left|\text{Im}\left\{T'_{23}\right\}\right| H\left(T'_{33} - \left|\text{Im}\left\{T'_{23}\right\}\right|\right)$
04: Calculate branch condition BC
05: Determine volume scattering model based on branch condition
06: Obtain volume scattering power $P_V = \left(2T'_{33} - P_C\right)/2c$
07: Compute parameters S, D, C_1, and C_2, as well as branch condition BC_1
08: Implement *SPAN* reservation ruling based on $S + D$
09: if $S + D > 0$

10:    Adaptively select between G4U and DG4U based on BC_1

11:    if $BC_1 > 0$

12:       $C = C_1$

13:    else

14:       $C = C_2$

15:    end if

16:    Calculate surface scattering power P_S and double-bounce scattering power P_D according to BC

17:    if $BC > 0$

18:       $P_S = S + |C|^2/S, P_D = D - |C|^2/S$

19:    else

20:       $P_S = S - |C|^2/D, P_D = D + |C|^2/D$

21:    end if

22:    Implement nonnegative P_S and P_D ruling

23: else

24:    $P_S = P_D = 0, P_V = T'_{11} + T'_{22} + T'_{33} - P_C$

25: end if

26: Output: P_S, P_D, P_V, P_C

4. Monitoring of disaster by EG4U decomposition of ALOS-PALSAR images of 2011 Tohoku tsunami/earthquake

As indicated in Subsection 3.4, G4U and S4R represent two special forms of GG4U of equal status. Hence, G4U cannot fully improve S4R only if we ascend the status of G4U by combining the duality of G4U, i.e., DG4U and G4U together for EG4U. EG4U can adaptively strengthen the surface scattering and double-bounce scattering. Therefore, it may improve the competence and performance of G4U in the remote sensing of damages caused by earthquake/tsunami disaster. We demonstrate these in the following by decomposing the ALOS-PALSAR images of the 2011 great Tohoku tsunami/earthquake using EG4U.

4.1 Great Tohoku earthquake and tsunami

The great Tohoku earthquake is also known as the great Sendai earthquake or the great East Japan earthquake, which was a magnitude 9.0–9.1 (Mw) undersea megathrust earthquake off the coast of northeast Japan (the epicenter is shown in **Figure 2** as "★") that occurred on March 11, 2011, the most powerful earthquake ever recorded in Japan [34]. The earthquake triggered powerful tsunami, which swept the mainland of Japan, killed over 10,000 people (mainly through drowning), and damaged over 1,000,000 buildings (half of them are collapsed and even totally collapsed) [35].

4.2 Datasets

The Advanced Land Observing Satellite (ALOS) was launched in 2006 by the Japanese Space Agency (JAXA). It has three remote sensing payloads, i.e., the Panchromatic Remote-sensing Instrument for Stereo Mapping (PRISM) for digital elevation mapping, the Advanced Visible and Near Infrared Radiometer type 2 (AVNIR-2) for precise land coverage observation, and the Phased Array type L-band SAR (PALSAR) for all-day/all-weather land observation [36].
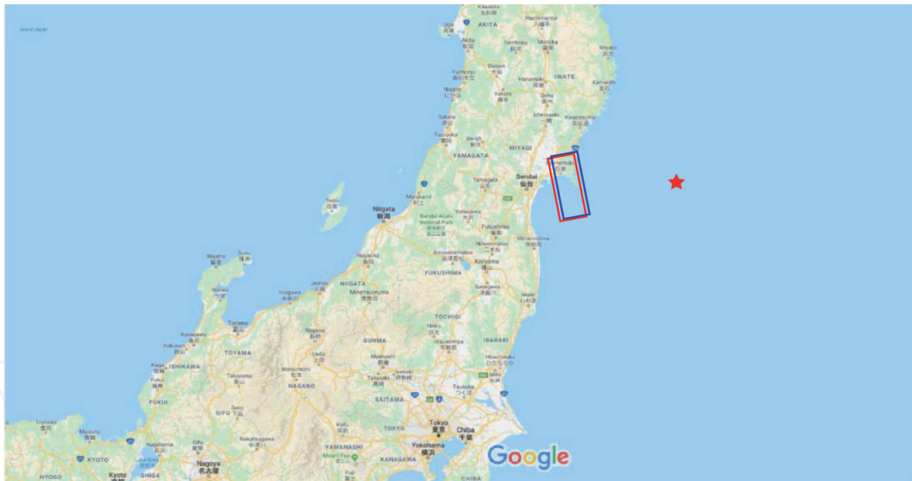
Figure 2.
Location of the great Tohoku tsunami/earthquake epicenter (★) and the ALOS-PALSAR footprint of the two selected fully polarimetric datasets (red rectangle, pre-event; blue rectangle, post-event).

Scene ID	Acquire data	Incidence angle[1]	Azimuth resolution	Ground-range resolution[2]
ALPSRP257090760	2010-11-21	23.802°	4.5 m	23.5 m
ALPSRP277220760	2011-04-08	23.836°	4.5 m	23.5 m

[1]*The incidence angle here indicates the incidence angle at the scene center.*
[2]*The ground-range resolution is defined as the slant-range resolution/sin(incidence angle) [9], while the slant-range resolution of the two datasets is both 9.5 m.*

Table 1.
ALOS-PALSAR datasets used in the experiment and their characteristics.

To demonstrate the capability of polarimetric remote sensing for damage monitoring, we choose two quad-polarization single-look complex-level 1.1 (ascending orbit) datasets acquired around Miyagi Prefecture, Japan, before and after the earthquake/tsunami with 138 days' temporal baseline, as summarized in **Table 1**. The ALOS-PALSAR footprint of the two datasets is shown in **Figure 2**.

4.3 Method

The flowchart of EG4U-based monitoring and evaluation of damages caused by tsunami/earthquake disaster is illustrated in **Figure 3**. We first co-register the two datasets based on the image features [37–40]. The boxcar filtering [9] is then carried out to both datasets to suppress the speckles. To ensure the pixel size in both image directions comparable, the window size for ensemble average is chosen as 2 pixels in ground-range direction and 12 pixels in azimuth direction, i.e., we integrate the scattering matrix $[S]$ of a total of 24 pixels for the estimation of a coherency matrix $\langle[T]\rangle$ in Eq. (2). From $\langle[T]\rangle$ we calculate the orientation angle θ according to Eq. (4) and implement the deorientation operation for the deoriented coherency matrix $\langle[T']\rangle$ according to Eq. (5). Finally, EG4U is used to decompose $\langle[T']\rangle$ to extract scattering powers P_S, P_D, P_V, and P_C and construct the RGB pseudo-color scattering power visualization result by encoding $\{R, G, B\}$ with $\{\sqrt{P_D}, \sqrt{P_V}, \sqrt{P_S}\}$. This process is executed on each cell of the two datasets until we obtain the complete pre- and post-event scattering power images shown in **Figure 4**, based on which we evaluate EG4U on monitoring of the tsunami/earthquake disaster in the following.
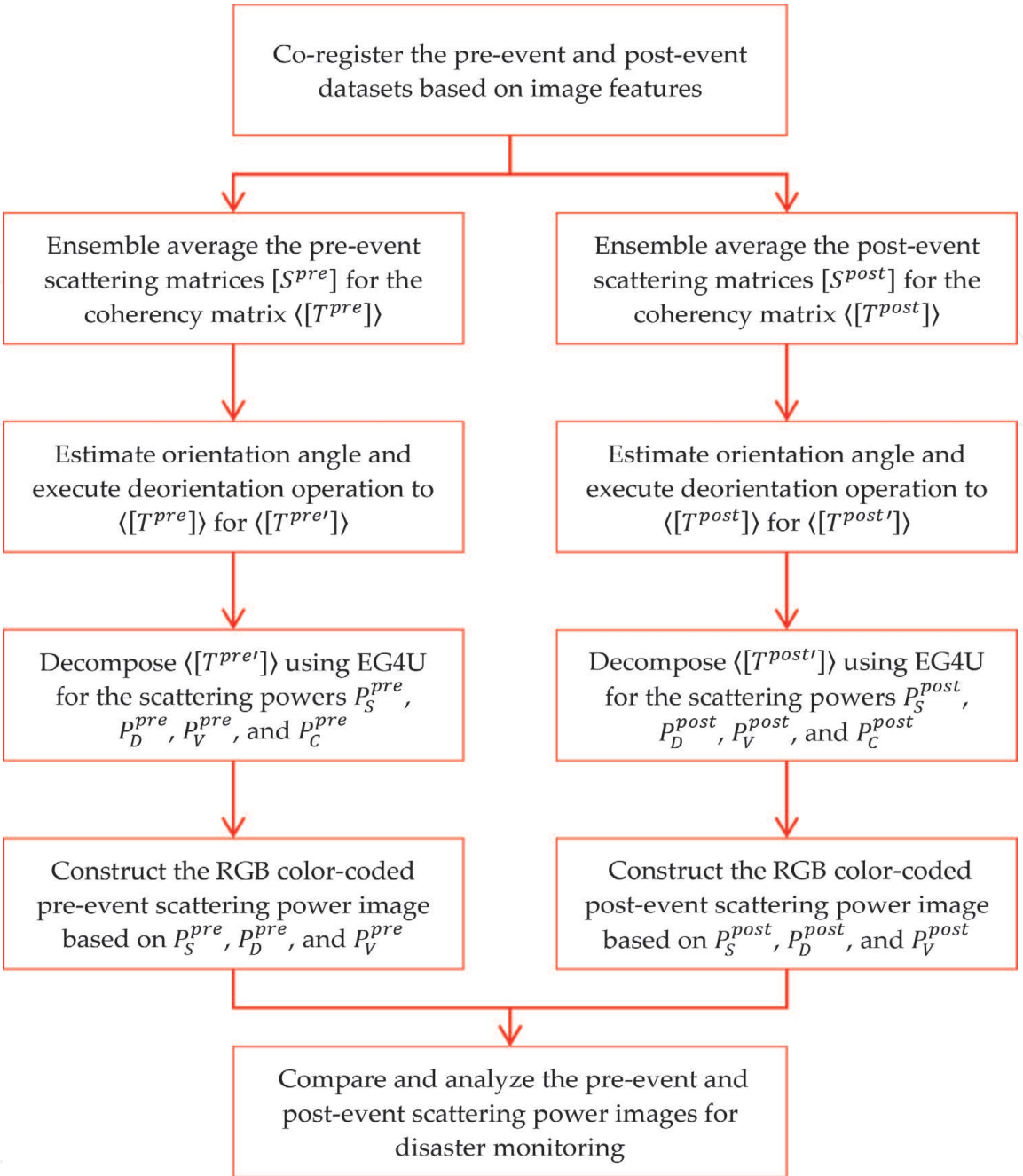
Co-register the pre-event and post-event datasets based on image features

Ensemble average the pre-event scattering matrices $[S^{pre}]$ for the coherency matrix $\langle[T^{pre}]\rangle$

Ensemble average the post-event scattering matrices $[S^{post}]$ for the coherency matrix $\langle[T^{post}]\rangle$

Estimate orientation angle and execute deorientation operation to $\langle[T^{pre}]\rangle$ for $\langle[T^{pre'}]\rangle$

Estimate orientation angle and execute deorientation operation to $\langle[T^{post}]\rangle$ for $\langle[T^{post'}]\rangle$

Decompose $\langle[T^{pre'}]\rangle$ using EG4U for the scattering powers P_S^{pre}, P_D^{pre}, P_V^{pre}, and P_C^{pre}

Decompose $\langle[T^{post'}]\rangle$ using EG4U for the scattering powers P_S^{post}, P_D^{post}, P_V^{post}, and P_C^{post}

Construct the RGB color-coded pre-event scattering power image based on P_S^{pre}, P_D^{pre}, and P_V^{pre}

Construct the RGB color-coded post-event scattering power image based on P_S^{post}, P_D^{post}, and P_V^{post}

Compare and analyze the pre-event and post-event scattering power images for disaster monitoring

Figure 3.
Flowchart of EG4U-based monitoring of tsunami/earthquake disaster.

4.4 Evaluation and analysis

For better comparison and analysis, we also display the optical image of the study area obtained from ©Google Earth in **Figure 5**. Our intuitive impression of **Figure 4(a)** and **(b)** is their consistency and nice correspondence to the optical image. The blue color mainly appears in the water and land areas because of the dominant surface scattering there. The red color mainly arises in the urban area, such as the Ishinomaki City and Higashi-Matsushima City, with a large number of buildings. The ground and the vertical walls of buildings constitute the dihedral corner structures, which generally reflect the dominant double-bounce scattering. Mountain presents the green color, i.e., the dominant volume scattering. The well-developed branch and crown structures of trees on the mountain complicate the scattering process, depolarize the scattering wave, and show themselves as the complex mixed volume scattering in PolSAR image. Therefore, by color-coding the
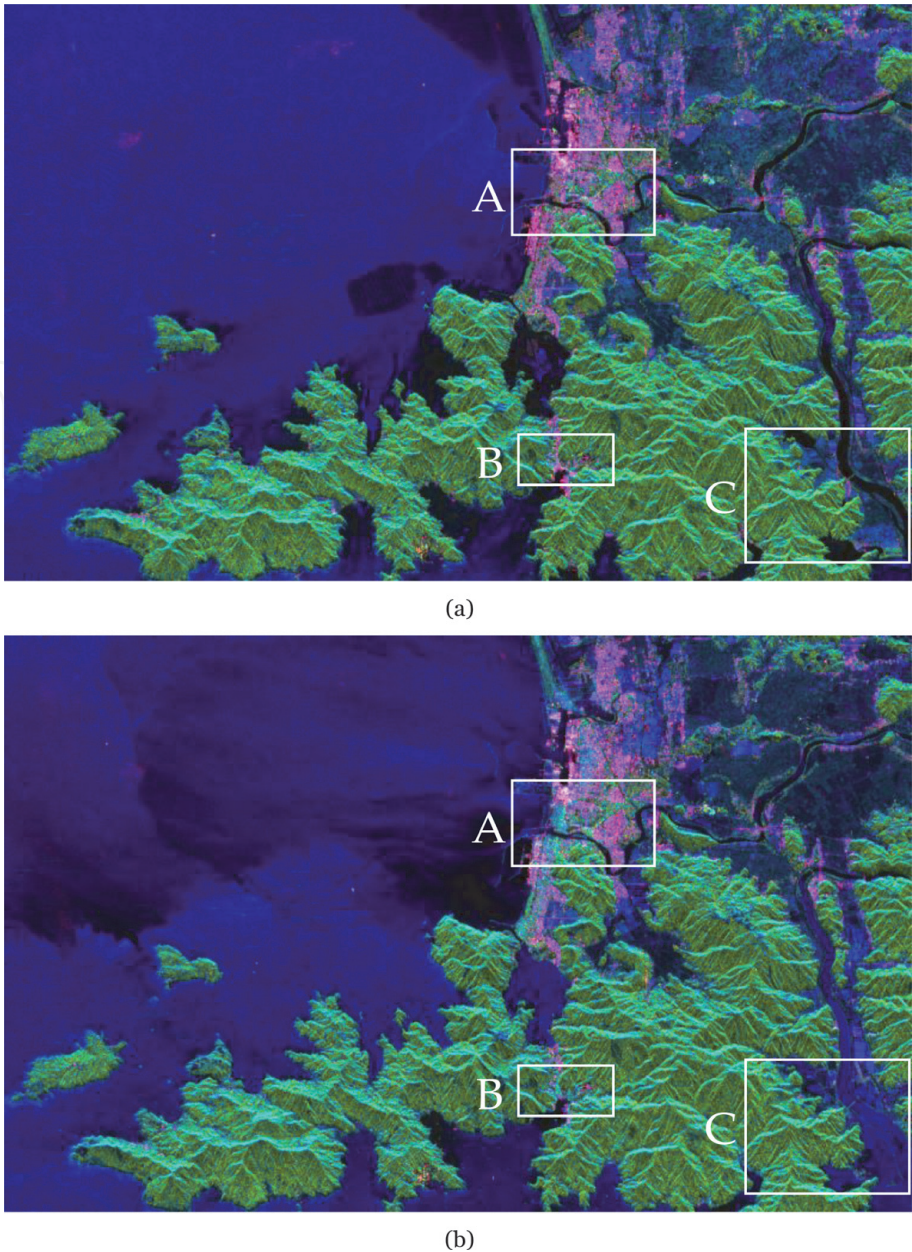
(a)

(b)

Figure 4.
Color-coded scattering power image of the study area (a) before and (b) after the great Tohoku tsunami/ earthquake disaster. The framed patch regions A, B, and C are extracted for particular analysis.

scattering powers obtained by EG4U, we can achieve a nice discrimination of the ground objects.

Despite the consistency, we can also observe the obvious difference between the pre- and post-event scattering power images. A lot of red pixels in **Figure 4(a)** change to blue pixels in **Figure 4(b)**, particularly in the urban areas of Ishinomaki and Higashi-Matsushima, which illustrate the change from the dominant double-bounce scattering to the dominant surface scattering, denote the decrease of the dihedral structures, and indicate the collapse of buildings. Take Ishinomaki City framed in Patch A for instance; it is interesting to observe that the strong change mainly arises in the area by the seaside, while tiny change occurs in the area away from the coast. This finding is also validated by the corresponding optical images acquired before and after the event shown in **Figure 6(a)** and **(b)**. Therefore, the severe damages brought by the Tohoku tsunami/earthquake are probably mainly due to the flooding rather than the earthquake. Flooding from the Onagawa Bay and the Mangokuura Sea also swept the town of Onagawa framed in Patch B,
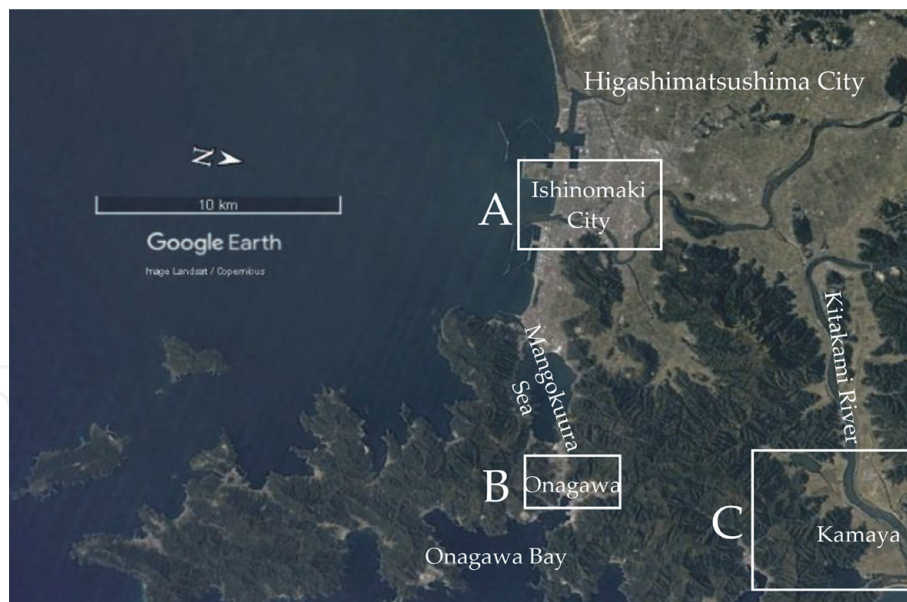
Figure 5.
Optical image of the study area obtained from ©Google earth. Particular attention is paid to the framed patch regions A, B, and C.

as shown in **Figure 6(c)** and **(d)** in terms of the pre- and post-event optical images. A large majority of red pixels of Patch B in **Figure 4(a)** change to blue pixels or even green pixels in **Figure 4(b)**, which indicates that nearly all the buildings in Onagawa were badly damaged by the flooding except for a few buildings constructed in high elevation. The collapsed buildings not only present the dominant surface scattering here, but also the dominant volume scattering because of the complex scattering in such mountain area. The biggest change caused by flooding appears in the area along the Kitakami River. Take the town of Kamaya framed in Patch C, for example, as shown in **Figure 6(e)**, besides several buildings, the most part of Kamaya is farmland. This area can be clearly distinguished from the Kitakami River in **Figure 4(a)** before the disaster. However, after the disaster, nearly all the land and buildings in Kamaya are flooded by the water from Kitakami River as shown in **Figure 6(f)**, which present in **Figure 4(b)** as the wide distribution of blue pixels and show the dominant surface scattering here. Therefore, by decomposing the pre- and post-event PolSAR datasets with EG4U to construct the color-coded scattering power images, we can achieve a simple but accurate monitoring of the damages caused by tsunami/earthquake disaster.

From the above analysis, we can obtain that flooding which resulted from tsunami is the main contributor to the severe damages in the 3.11 great Tohoku earthquake. The flooding destroyed the buildings and inundated the lands. All these damages present themselves in the polarization domain as the change of the dominant scattering mechanism from double-bounce scattering to surface scattering and in the image domain as the change of pixel color from red to blue. The boundary condition BC has been widely used in model-based decomposition as a crucial feature to discriminate surface scattering and double-bounce scattering [23, 24, 26–28]. As expressed in Eq. (14), $BC > 0$ indicates stronger surface scattering than double-bounce scattering, while $BC \leq 0$ denotes stronger double-bounce scattering than surface scattering. Therefore, besides the qualitative evaluation in terms of color, we can further achieve an quantitative evaluation of the damages by analyzing the dominant scattering according to BC. **Figure 7(a)** and **(b)** show the binary images of BC before and after the disaster, respectively. The white pixel denotes $BC > 0$, i.e., the dominant surface scattering, which mainly occupies the water and land areas, while the black one denotes $BC \leq 0$, i.e., the dominant double-bounce

Figure 6.
Optical images of (first row, i.e. (a) and (b)) patch A, (second row, i.e. (c) and (d)) patch B, and (third row, i.e. (e) and (f)) patch C obtained from ©Google earth (first column, i.e. (a), (c), and (e)) before and (second column, i.e. (b), (d), and (f)) after the 3.11 great Tohoku tsunami/earthquake.

scattering, which mainly occupies the urban and mountain areas. Before disaster, the black pixels account for 15.1641% of the whole image, while this ratio decreases to 13.0785% after the disaster, i.e., the dominant scattering mechanism of about 2.0856% area of the scene is changed from double-bounce scattering to surface scattering. As shown in **Figure 7**, the change mainly arises in the urban area like the Ishinomaki City and Higashi-Matsushima City, in the land area like the town of Kamaya, as well as in the water area like the Mangokuura Sea, Onagawa Bay, and Kitakami River. This further provides us a consistently quantitative evaluation of the damages. All these demonstrate the importance and value of polarimetric microwave remote sensing technique in the monitoring of tsunami/earthquake damages.

Singh et al. [28] indicated that G4U could enhance double-bounce scattering over urban area while strengthen surface scattering contribution over water and land area. This establishes G4U the state-of-the-art four-component scattering
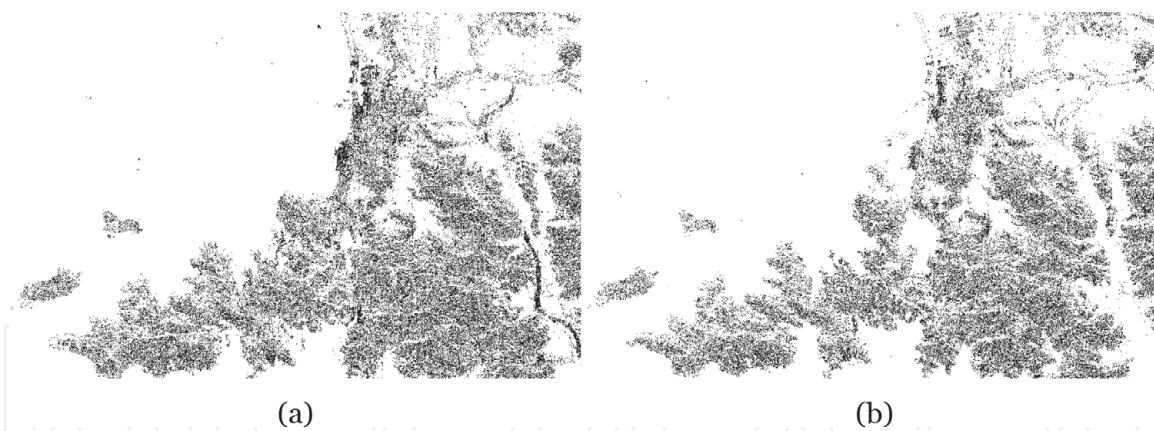
Figure 7.
Binary display of the branch condition BC extracted from (a) pre- and (b) post-event ALOS-PALSAR datasets. The white pixels correspond to BC > 0, while the black pixels denote BC ≤ 0.

Figure 8.
Binary display of the branch condition BC_1 extracted from (a) pre- and (b) post-event ALOS-PALSAR datasets. The white pixels correspond to $BC_1 > 0$, while the black pixels denote $BC_1 \leq 0$.
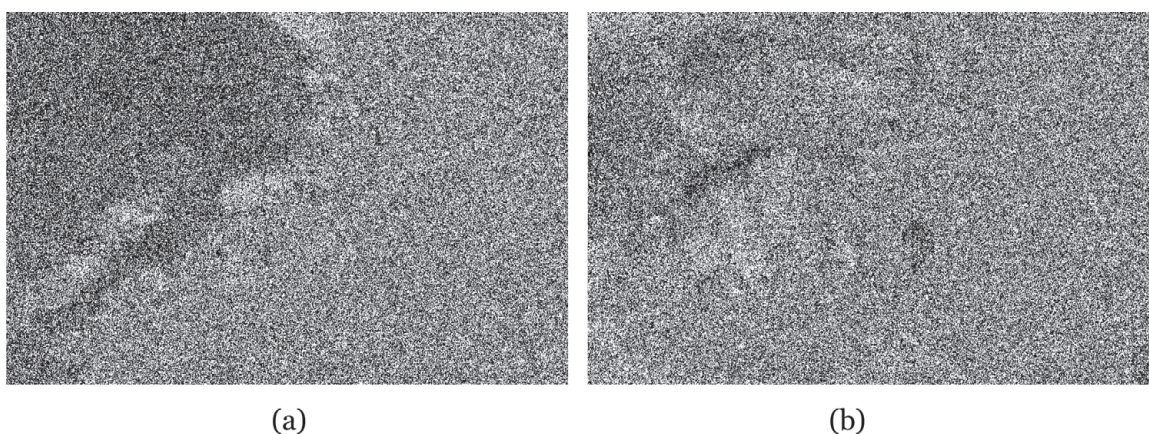
power decomposition and enables its wide application to the remote sensing of forestry, agriculture, wetland, snow, glaciated terrain, earth surface, manmade target, environment, and damages caused by earthquake, tsunami, and landslide [29, 30]. Nevertheless, the rigorous derivation in Eq. (21) validates that G4U cannot always enhance the double-bounce scattering nor strengthen the surface scattering power unless we adaptively integrate G4U and its duality, i.e., DG4U, for EG4U based on another boundary condition BC_1. As expressed in Eq. (27), G4U is selected only when $BC_1 > 0$; otherwise, we should turn to DG4U. The binary images **Figure 8(a)** and **(b)** further show the pre- and post-event BC_1, respectively, where the white pixels (i.e., $BC_1 > 0$) indicate the area where G4U operates and the black pixels (i.e., $BC_1 \leq 0$) give the area where DG4U operates. The white pixels account for 46.4260% of the pre-event image, which conveys that G4U achieves better result than S4R only for 46.4260% area. As for the rest 53.5740% area, we should resort to DG4U for improvement. The ratio of white pixels increases to 49.5247% after the disaster. Nevertheless, there are still half a little more areas where G4U will underestimate the surface or double-bounce scattering. If we adopt G4U in this area to evaluate damages caused by tsunami/earthquake, the reduced double-bounce scattering from G4U may lead to the underestimation of building scale and overestimation of damage level. EG4U can adaptively increase the surface scattering or double-bounce scattering. Hence, it definitely improves the competence and performance of G4U in the remote sensing of damages caused by earthquake/tsunami.

5. Conclusion

Flooding is the main contributor to the severe damages in the great Tohoku tsunami/earthquake. It destroyed the buildings and inundated the lands by the seaside. All these damages present themselves in the polarization domain as the change of the dominant scattering mechanism from double-bounce scattering to surface scattering and in the image domain as the change of pixel color from red to blue. The color-coded scattering power image is very useful and powerful in the qualitative evaluation of damages. The boundary condition BC further enables a nice quantitative evaluation of disaster. The unitary transformation in G4U adds a T_{13}-related but redundant balance equation to the original self-contained equation system. The general solution enables a generalized G4U, while G4U just represents a special form. The strict derivation conveys that G4U cannot always strengthen the double-bounce scattering in urban area nor strengthen the surface scattering in water or land area unless we adaptively combine G4U and its duality for EG4U. Experiment on the ALOS-PALSAR datasets of 2011 great Tohoku tsunami/earthquake demonstrates not only the outperformance of EG4U but also the effectiveness of polarimetric remote sensing in the qualitative monitoring and quantitative evaluation of tsunami/earthquake damages. Efficient and accurate monitoring and assessment are of crucial importance for the fast response, management, and mitigation of the disasters. The all-day and all-weather working capacity is a significant advantage of microwave remote sensing. Polarimetric remote sensing is an effective technique in the discrimination and recognition of ground objects.

Acknowledgements

Conflict of interest

The authors declare no conflict of interest.

Notes

Sections 2 and 3 of this chapter are extracted from a journal paper of the authors submitted to IEEE Transactions on Geoscience and Remote Sensing on June 07, 2017. The paper is still under review at the time of publication of this chapter. For more details about the paper, please refer to Reference [30].

Author details

Dong Li[1,2]*, Yunhua Zhang[1,2]*, Liting Liang[1,2], Jiefang Yang[1] and Xun Wang[1,2]

1 Key Laboratory of Microwave Remote Sensing, National Space Science Center, Chinese Academy of Sciences, Beijing, China

2 University of Chinese Academy of Sciences, Beijing, China

*Address all correspondence to: lidong@mirslab.cn and zhangyunhua@mirslab.cn

IntechOpen

References

[1] Mokhtari M, editor. Tsunami-A Growing Disaster. London: IntechOpen; 2011. p. 232. DOI: 10.5772/922

[2] Morner N-A, editor. The Tsunami Threat–Research and Technology. London: IntechOpen; 2011. p. 714. DOI: 10.5772/573

[3] Mokhtari M, editor. Tsunami. London: IntechOpen; 2016. p. 164. DOI: 10.5772/61999

[4] Marghany M, editor. Advanced Remote Sensing Technology for Synthetic Aperture Radar Applications, Tsunami Disasters, and Infrastructure. London: IntechOpen; 2019. p. 167. DOI: 10.5772/intechopen.78525

[5] Li D, Zhang Y. Adaptive model-based classification of PolSAR data. IEEE Transactions on Geoscience and Remote Sensing. 2018;**56**(12):6940-6955. DOI: 10.1109/TGRS.2018.2845944

[6] Li D, Zhang Y. Random similarity-based entropy/alpha classification of PolSAR data. IEEE Journal of Selected Topics in Applied Earth Observations and Remote Sensing. 2017;**10**(12): 5712-5723. DOI: 10.1109/JSTARS.2017.2748234

[7] Li D, Zhang Y. Unified Huynen phenomenological decomposition of radar targets and its classification applications. IEEE Transactions on Geoscience and Remote Sensing. 2016; **54**(2):723-743. DOI: 10.1109/TGRS.2015.2464113

[8] Li D, Zhang Y. Random similarity between two mixed scatterers. IEEE Geoscience and Remote Sensing Letters. 2015;**12**(12):2468-2472. DOI: 10.1109/LGRS.2015.2484383

[9] Lee J-S, Pottier E. Polarimetric Radar Imaging: From Basics to Applications. Boca Raton: CRC Press; 2009. p. 422. DOI: 10.1201/9781420054989

[10] Cloude SR. Polarisation Applications in Remote Sensing. Oxford: Oxford University Press; 2010. p. 453. DOI: 10.1063/1.3502550

[11] van Zyl JJ, Kim Y. Synthetic Aperture Radar Polarimetry. Hoboken: John Wiley & Sons, Inc.; 2011. p. 312. DOI: 10.1002/9781118116104

[12] Yamaguchi Y. Disaster monitoring by fully polarimetric SAR data acquired with ALOS-PALSAR. Proceedings of the IEEE. 2012;**100**(10):2851-2860. DOI: 10.1109/JPROC.2012.2195469

[13] Sato M, Chen S-W, Satake M. Polarimetric SAR analysis of tsunami damage following the march 11, 2011 East Japan earthquake. Proceedings of the IEEE. 2012;**100**(10):2861-2875. DOI: 10.1109/JPROC.2012.2200649

[14] Watanabe M, Motohka T, Miyagi Y, Yonezawa C, Shimada M. Analysis of urban areas affected by the 2011 off the Pacific coast of Tohoku earthquake and tsunami with L-band SAR full-polarimetric mode. IEEE Geoscience and Remote Sensing Letters. 2012;**9**(3): 472-476. DOI: 10.1109/LGRS.2011.2182030

[15] Li X, Zhang L, Guo H, Sun Z, Liang L. New approaches to urban area change detection using multitemporal RADARSAT-2 polarimetric synthetic aperture radar (SAR) data. Canadian Journal of Remote Sensing. 2012;**38**(3): 253-255. DOI: 10.5589/m12-018

[16] Singh G, Yamaguchi Y, Boerner W-M, Park S-E. Monitoring of the March 11, 2011, off-Tohoku 9.0 earthquake with super-tsunami disaster by implementing fully polarimetric high-resolution POLSAR techniques.

Proceedings of the IEEE. 2013;**101**(3): 831-846. DOI: 10.1109/JPROC.2012. 2230311

[17] Chen S-W, Sato M. Tsunami damage investigation of built-up areas using multitemporal spaceborne full polarimetric SAR images. IEEE Transactions on Geoscience and Remote Sensing. 2013;**51**(4):1985-1997. DOI: 10.1109/TGRS.2012.2210050

[18] Li N, Wang R, Deng Y, Liu Y, Wang C, Balz T, et al. Polarimetric response of landslides at X-band following the Wenchuan earthquake. IEEE Geoscience and Remote Sensing Letters. 2014;**11**(10):1722-1726. DOI: 10.1109/LGRS.2014.2306820

[19] Chen S-W, Wang X-S, Sato M. Urban damage level mapping based on scattering mechanism investigation using fully polarimetric SAR data for the 3.11 East Japan earthquake. IEEE Transactions on Geoscience and Remote Sensing. 2016;**54**(12):6919-6929. DOI: 10.1109/TGRS.2016.2588325

[20] Ji Y, Sumantyo JTS, Chua MY, Waqar MM. Earthquake/tsunami damage level mapping of urban areas using full polarimetric SAR data. IEEE Journal of Selected Topics in Applied Earth Observations and Remote Sensing. 2018;**11**(7):2296-2309. DOI: 10.1109/JSTARS.2018.2822825

[21] Zhai W, Huang C, Pei W. Two new polarimetric feature parameters for the recognition of the different kinds of buildings in earthquake-stricken areas based on entropy and eigenvalues of PolSAR decomposition. Remote Sensing. 2018;**10**(10):1613. DOI: 10.3390/ rs10101613

[22] Cloude SR, Pottier E. A review of target decomposition theorems in radar polarimetry. IEEE Transactions on Geoscience and Remote Sensing. 1996; **34**(2):498-518. DOI: 10.1109/36.485127

[23] Freeman A, Durden SL. A three-component scattering model for polarimetric SAR data. IEEE Transactions on Geoscience and Remote Sensing. 1998;**36**(3):963-973. DOI: 10.1109/36.673687

[24] Yamaguchi Y, Moriyama T, Ishido M, Yamada H. Four-component scattering model for polarimetric SAR image decomposition. IEEE Transactions on Geoscience and Remote Sensing. 2005;**43**(8):1699-1706. DOI: 10.1109/TGRS.2005.852084

[25] Zhu F, Zhang Y, Li D. A novel deorientation method in PolSAR data processing. Remote Sensing Letters. 2016;**7**(11):1083-1092. DOI: 10.1080/ 2150704X.2016.1217438

[26] Yamaguchi Y, Sato A, Boerner W-M, Sato R, Yamada H. Four-component scattering power decomposition with rotation of coherency matrix. IEEE Transactions on Geoscience and Remote Sensing. 2011;**49**(6):2251-2258. DOI: 10.1109/TGRS.2010.2099124

[27] Sato A, Yamaguchi Y, Singh G, Park S-E. Four-component scattering power decomposition with extended volume scattering model. IEEE Geoscience and Remote Sensing Letters. 2012;**9**(2):166-170. DOI: 10.1109/LGRS. 2011.2162935

[28] Singh G, Yamaguchi Y, Park S-E. General four-component scattering power decomposition with unitary transformation of coherency matrix. IEEE Transactions on Geoscience and Remote Sensing. 2013;**51**(5):3014-3022. DOI: 10.1109/TGRS.2012.2212446

[29] Li D, Zhang Y, Liang L. A Concise Survey of G4U. 2019. Available from: https://arxiv.org/ftp/arxiv/papers/1910/ 1910.14323.pdf [Accessed: 28 December 2019]

[30] Li D, Zhang Y, Liang L. A mathematical extension to the general

four-component scattering power decomposition with unitary transformation of coherency matrix. IEEE Transactions on Geoscience and Remote Sensing. 2020:1-18. Under review

[31] Sinclair G. The transmission and reception of elliptically polarized waves. Proceedings of the IRE. 1950;**32**(2): 148-151. DOI: 10.1109/JRPROC.1950. 230106

[32] Huynen JR. Phenomenological theory of radar targets [thesis]. Delft: Delft University of Technology; 1970

[33] Cloude SR, Pottier E. An entropy based classification scheme for land applications of polarimetric SAR. IEEE Transactions on Geoscience and Remote Sensing. 1997;**35**(1):68-78. DOI: 10.1109/36.551935

[34] Wikipedia. 2011 Tohoku Earthquake and Tsunami. 2019. Available from: https://en.wikipedia. org/wiki/2011_T%C5%8Dhoku_ earth quake_and_tsunami. [Accessed: 28 December 2019]

[35] National Police Agency of Japan. Police Countermeasures and Damage Situation associated with 2011 Tohoku district-off the Pacific Ocean Earthquake. 2019. Available from: https://www.npa.go.jp/news/other/ earthquake2011/pdf/higaijokyo_e.pdf [Accessed: 28 December 2019]

[36] JAXA Earth Observation Research Center. About ALOS–Overview and Objectives. 2019. Available from: https://www.eorc.jaxa.jp/ALOS/en/ about/about_index.htm [Accessed: 28 December 2019]

[37] Li D, Zhang Y. A novel approach for the registration of weak affine images. Pattern Recognition Letters. 2012; **33**(12):1647-1655. DOI: 10.1016/j. patrec.2012.04.009

[38] Li D, Zhang Y. A fast offset estimation approach for InSAR image subpixel registration. IEEE Geoscience and Remote Sensing Letters. 2012;**9**(2): 267-271. DOI: 10.1109/LGRS.2011. 2166752

[39] Li D, Zhang Y. On the appropriate feature for general SAR image registration. Proceedings of SPIE. 2012; **8536**:8536X. DOI: 10.1117/12.970520

[40] Li D, Zhang Y. The appropriate parameter retrieval algorithm for feature-based SAR image registration. Proceedings of SPIE. 2012;**8536**:8536Y. DOI: 10.1117/12.970522